J. Fluid Mech. (2001), *vol.* 443, *pp.* 1–25. Printed in the United Kingdom

Transverse jets and jet flames. Part 1. Scaling laws for strong transverse jets

By ERNEST F. HASSELBRINK JR† AND M. G. MUNGAL

Mechanical Engineering Department, Stanford University, Stanford, CA 94305-3032, USA

(Received 15 March 2000 and in revised form 13 September 2000)

We present a similarity analysis of strong turbulent jets directed perpendicularly into a crossflow. The analysis neglects pressure terms in the governing equations, and assumes complete similarity in each of two intermediate-asymptotic regions of the flow: a jet region, where the jet is largely unaffected by the crossflow, and a wake-like region, where the jet has been deflected well into the crossflow. Scaling laws are derived for velocity, scalar concentration, and jet trajectory, and show good agreement with existing experimental data. The structure of the counter-rotating vortex pair implied by this analysis is significantly different from typical representations found in the literature.

1. Introduction

The turbulent transverse jet is a simple flow configuration wherein a jet of fluid issues perpendicular to a uniform crossflow. It is found in a wide variety of industrial and aerospace applications, such as industrial burners, pipe tee mixers, flare stacks, and vertical take-off/landing aircraft. However, when engineers design systems incorporating transverse jets, they do so without the benefit of a theoretical and experimental knowledge base akin to that existing for free and coflowing jets, namely: (i) a similarity theory, (ii) a corresponding set of scaling laws for velocity and scalar averages/fluctuations, and (iii) experimentally determined profiles and coefficients. This paper is an attempt to remedy these shortcomings in our understanding of transverse jets.

To this end, Part 1 of this paper presents a similarity theory, which is essentially a synthesis of transverse jet scaling ideas of Broadwell & Breidenthal (1984) and intermediate asymptotics theory of Barenblatt & Zel'dovich (1972) and Barenblatt (1996). The results are compared to recently reported data for the mixture fraction field and previous work on the velocity field. Implications for the structure of the vorticity field are also considered. Part 2 (Hassebrink & Mungal 2001) presents new particle image velocimetry data, which verifies the scalings presented in Part 1, and also considers the modification of the flow field due to combustion heat release. It also provides a glimpse of flow complexities not accessible by a simple scaling law theory.

2. Previous work

2.1. *Vorticity field structure*

The transverse jet has become an example of turbulent flow composed of 'coherent structures' – dominant vortical systems, which have offered the hope of a mechanistic,

† Present address: Department of Mechanical Engineering, University of Michigan, Ann Arbor, MI 48109-2121, USA.

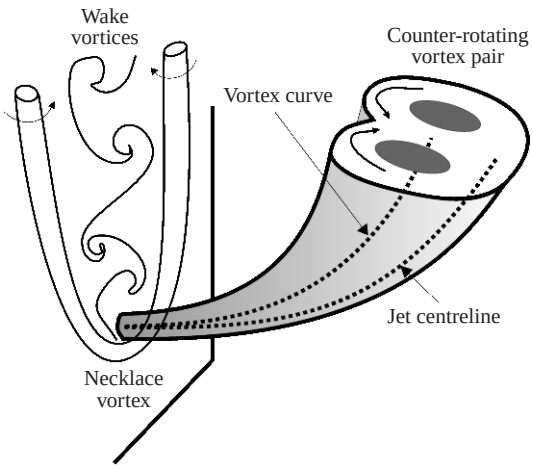

FIGURE 1. Features of the transverse jet, adapted from Margason (1993). The jet is characterized by a jet shear layer, a horseshoe vortex system, 'wake' vortices, and a dominant counter-rotating vortex pair. Only a cross-section of the wake vortices is shown at the wall, but they extend horizontally from the wall into the vortex pair.

rather than statistical, understanding of turbulence. There are four main transverse jet vortical systems, as described in detail by Fric & Roshko (1994), and these are shown schematically in figure 1, adapted from Margason (1993). The jet initially issues in the $+x$-direction, into a crossflow in the $+y$-direction. The jet is characterized by the jet shear layer observed in free jets, and three additional unsteady vortical systems: a 'horseshoe' or 'necklace' vortex, a street of 'wake vortices', and a 'counter-rotating vortex pair' (CVP), which has received the majority of the research attention.

The structure of the CVP is a possible source of confusion. Despite the 'classical' portrayal of the CVP in figure 1, it is generally agreed that the CVP is not simply a pair of vortex tubes which extend from the jet nozzle into the crossflow (i.e. with a local flux-averaged vorticity vector which is approximately parallel to the local jet trajectory). This view of the CVP is merely a simplified interpretation of time-averaged data obtained in the CVP cross-section (Scorer 1958; Kamotani & Greber 1972; Fearn & Weston 1974), and a useful modelling tool. A more sophisticated view was originally suggested by Moussa, Trischka & Eskinazi (1977), who studied the roll-up of vorticity at the jet shear layer, and identified it as the primary source of vorticity in the CVP. In analysing the convective acceleration equation of a vortex ring shedding from the nozzle, they noted:

> In time, the ring will be swept with the fluid, decelerating on the windward side faster than at the centre and accelerating relatively on the lee side. This situation will persist with diminishing intensity during the entire development of the deflected jet as it asymptotically approaches a Beltrami flow …

In other words, rings rotate *towards* the crossflow as they are swept away by it. Several investigations (Coelho & Hunt 1989; Andreopoulos & Rodi 1985; Sykes, Lewellen & Parker 1986; Broadwell & Breidenthal 1984; Fric & Roshko 1994; Kelso, Lim & Perry 1996) present measurements, calculations, and analysis supporting this general conclusion. The effect is seen in the vortex lines plotted in the computation by Sykes *et al.* (1986), in flow visualization of pulsed transverse jets (Eroglu & Breidenthal 1991), and in an experiment where individual vortex rings were injected into a crossflow

(Chang & Vakili 1995). In § 5 we too will show, through consideration of the first moment of the vorticity, that this behaviour can be interpreted as a simple result of momentum conservation. Furthermore, the angle of inclination towards the crossflow (in the limit of ideal point-vortex cores) must be constant throughout the CVP.

Detailed velocity and vorticity field measurements in the CVP cross-section have been performed by several investigators (Kamotani & Greber 1972; Fearn & Weston 1974; Moussa *et al.* 1977; Kuzo 1995) for jets with blowing ratios as high as $r = 20$. Measurements of the velocity field in the symmetry plane have also been performed by several previous studies (Patrick 1967; Chassaing *et al.* 1974; Andreopoulos & Rodi 1985; Kelso *et al.* 1996; Gogineni, Goss & Roquemore 1995). However, only the results of Patrick (1967) present detailed velocity fields for $r > 8$. Other studies (Coelho & Hunt 1989; Kelso *et al.* 1996) address the details of the streamline topology near the jet nozzle. The data set in the present work complements previous velocity field measurements by providing symmetry-plane data for $r = 10$ and $r = 21$.

2.2. *Jet trajectory*

The arc subtended in space by the centre streamline of a transverse jet is a fundamental characteristic of interest. However, data on transverse jet trajectories show significant scatter, partly due to differing definitions of the jet centreline, partly from differing experimental apparatus, and partly from differing opinions on the best form of the correlating equation. Margason (1968) reviewed several published correlations, and concluded that much of the data could be collapsed by normalizing coordinates with the product rd, leading to a simple power-law trajectory:

$$\frac{y}{rd} = A\left(\frac{x}{rd}\right)^B. \tag{2.1}$$

Here A is a constant, approximately equal to 1.6, B is a constant, approximately $1/3$, and r is a flow parameter called the *blowing ratio*, usually taken as

$$r = \left(\frac{\rho_j u_j^2}{\rho_\infty v_\infty^2}\right)^{1/2}, \tag{2.2}$$

where subscript j denotes properties at the jet nozzle and subscript ∞ those in the undisturbed crossflow. An extensive table of experimental values for A and B (although cast in another form) are reported in Margason (1993). An oft-cited result is $A = 2.05$, $B = 0.28$ (Pratte & Baines 1967); however, values are reported in the literature in the range $1.2 < A < 2.6$, and $0.28 < B < 0.34$, indicating considerable scatter in the values of the coefficients.

Some of the scatter stems from the determination of u_j, which is a spatial variable at the jet exit. The numerator in (2.2) is best defined in terms of an integral conserved quantity, e.g. such as the average momentum flux per unit area of the jet, J/A_j, which is equal to the numerator only in the case of perfectly uniform jet exit velocity.

Another source of scatter in the data can be explained by the discovery by Kamotani & Greber (1972) that the trajectory of maximum velocity penetrates further into the crossflow than the trajectory based on maximum concentration. Furthermore, their results show A to be a function of r; e.g. when their trajectories are cast in the more general form

$$\frac{y}{rd} = Ar^C\left(\frac{x}{rd}\right)^B, \tag{2.3}$$

they find $C = 0.30$. Similar results were also found by Smith & Mungal (1998), who obtained extensive scalar concentration data for jets with $5 < r < 25$.

Equation (2.1), with $B = 1/3$, is the trajectory correlation obtained in the self-similarity analysis by Broadwell & Breidenthal (1984). The data supporting (2.3) would therefore seem to imply that similarity assumptions are not valid. In the present work, we will demonstrate that the assumptions leading to the trajectory given in (2.1) require that $r \gg 1$.

2.3. *Analytical approaches*

The analytical portion of the present work is similar to the work of Broadwell & Breidenthal (1984). There, the observation is made that in the very far field (where the jet is almost completely deflected into the crossflow), the jet essentially becomes a counter-rotating vortex pair, translating in the crossflow. By noting that turbulent vortex pairs have a characteristic width proportional to wall-normal distance, they derive far-field scaling laws for characteristic quantities of interest. The present work arrives at the same conclusions for the very far field by different means, but also provides suggestions for the behaviour closer to the jet nozzle. We note that Abramovich (1963) assumes that jet width is proportional to jet arc length (as opposed to wall-normal distance), which matches the data in the slightly deflected region reasonably well, but poorly matches the far-field data, where the jet is nearly parallel to the crossflow.

There are also several analyses in the literature which obtain closure by incorporating some assumption about the jet entrainment rate. Hoult & Weil (1972) deal with the more general problem of buoyant turbulent jets, and assume that entrainment rate is proportional to the local shear velocity (with differing coefficients for buoyancy-driven and momentum-driven shear). They predict the existence of critical buoyancy and momentum length scales, where the plume trajectory transitions to different power-law scaling; the theory is shown to match the accumulated data. Another entrainment analysis is presented by Keffer & Baines (1963). However, they identify the outer momentum length scale as $r^2 d$, and a later study by Pratte & Baines (1967), with extensive supporting data, finds it to be rd.

Another interesting theoretical approach has been to consider the kinematics of the vorticity field. The near field of strong jets has been studied by Coelho & Hunt (1989), who perform a perturbation analysis on the annular vortex sheet issuing from the nozzle into a crosswind. They conclude that the sheet deforms three-dimensionally in response to the pressure field, but does not deflect in the crossflow. They propose that jet deflection is caused by entrainment into the sheet, and demonstrate that the sheet does indeed deflect once entrainment is added to the model. Another kinematic model by Karagozian (1986) considers the motion of a quasi-two-dimensional vortex pair which issues from the jet nozzle and interacts with the crosswind. The analysis has been used to predict flame lengths (Karagozian & Nguyen 1986) as well as the jet width and trajectory, with reasonable agreement to data.

3. Similarity analysis

3.1. *Conservation equations applied to the transverse jet*

The first step is to identify the invariants of the flow, by applying conservation equations to a control volume such as that shown in figure 2. The distance along the centreline trajectory is denoted by s; each point along s is uniquely mapped to a coordinate position (x_c, y_c). The velocity field $\boldsymbol{u}$ has components u, v and w; in this

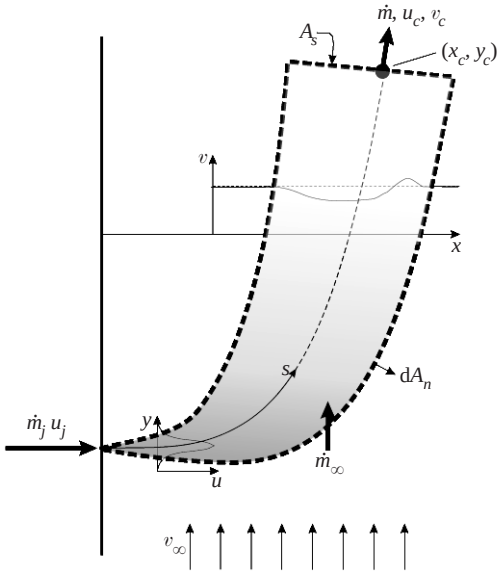

FIGURE 2. Control-volume for analysis of transverse jets. The origin of coordinates x, y and s is at the centre of the jet exit. A_s denotes the cross-sectional area at a distance s along the trajectory; $\mathrm{d}A_n$ denotes a unit-area outward normal vector.

analysis we are primarily concerned with velocity components u and v. We assume for the moment that the velocity field is approximately parallel to $\boldsymbol{s}$ in regions near the centreline.

With these approximations, it is possible to express the mass flux, x-momentum flux, and y-momentum deficit through the cross-section at a given distance x from the nozzle, using A_s to denote the cross-section area as, respectively,

$$\dot{m}(s) = \int_{A_s} \rho \sqrt{(u^2 + v^2)}\, \mathrm{d}A_s, \tag{3.1}$$

$$J(s) = \int_{A_s} \rho u \sqrt{(u^2 + v^2)}\, \mathrm{d}A_s, \tag{3.2}$$

$$\theta(s) = \int_{A_s} \rho (v - v_\infty) \sqrt{(u^2 + v^2)}\, \mathrm{d}A_s. \tag{3.3}$$

We now take inspiration from the smoke-wire visualizations of Fric & Roshko (1994), which show that crossflow streaklines approaching the jet remain almost completely unperturbed until they reach the turbulent vortices within it (in contrast with streaklines around a cylinder, which diverge well upstream of the cylinder). Thus we assume that the jet's perturbation to the crossflow is confined to the characteristic area A_s, and that outside this area, $u \to 0$ and $v \to v_\infty$. Hence, by drawing the control volume just outside the jet, flux integrals which would normally extend over infinite planes (or half-planes) may be restricted to A_s, because there is no contribution to the x-momentum or to the deficit of y-momentum outside A_s. Conservation of mass, and balance of momentum can then be expressed

$$\dot{m}(s) = \dot{m}_j + \dot{m}_\infty(s), \tag{3.4}$$

$$J(s) = J_j + \int_{A_n} P(\mathrm{d}A_n \cdot \hat{\boldsymbol{x}}), \tag{3.5}$$

$$\theta(s) = \theta_j + \int_{A_n} P(\mathrm{d}A_n \cdot \hat{\boldsymbol{y}}), \tag{3.6}$$

where P is the pressure, and $\hat{\boldsymbol{x}}$ and $\hat{\boldsymbol{y}}$ are unit vectors in the x- and y-directions. The assumption that $u \to 0$ and $v \to v_\infty$ outside A_s implies that shear stress is zero on the surface of the control volume, so no terms are included to account for this effect.

It would now be convenient to eliminate the pressure terms from equations (3.4)–(3.6); fortunately, previous work has provided justification of this when $r \gg 1$. Wall pressure measurements (Fearn & Weston 1975) show a low-pressure region at the lee of the jet exit, and a smaller high-pressure region on the windward side of it. The measurements show that a net lift force is exerted on the wall, of the form $c_L \rho_\infty v_\infty^2 d^2 \phi(r)$. Here c_L is a lift coefficient, and $\phi(r)$ is a function which behaves as $\phi(r \to 0) \to 0$, $\phi(r \to \infty) \to 1$. By integrating the wall pressure coefficient contours for high-r cases, we estimate that the lift coefficient asymptotically approaches $c_L \approx -10$. Therefore, the ratio of the pressure term in (3.5) to J_j (the left-hand side) is $\sim 10/r^2$, i.e. the pressure term in (3.5) is negligible for $r \geqslant 10$ (although it should be noted that wall pressure coefficients were highest near the jet nozzle; hence the assumption that pressure terms are negligible is less valid near the nozzle). For the crossflow direction (3.6), the inviscid and viscous analyses for strong jets by Coelho & Hunt (1989) concluded that jet deflection was entirely governed by entrainment into the jet, not by pressure effects. Hence we neglect the pressure term in (3.6) as well (again, with the requirement that $r \gg 1$). However, we emphasize that this remains an assumption, the validity of which remains to be seen in the data.

Dropping the pressure terms, the momentum balances imply that there are two invariants of the flow: $J = J_j$ ($\approx \dot{m}_j u_j$) and $\theta = \theta_j$ ($\approx \dot{m}_j v_\infty$). Since these are invariants, henceforth the subscripts and dependences on s are dropped. It is noted that the presence of two invariants usually precludes the existence of a similarity solution. General scaling principles have been found for shear flows with a single invariant (Cantwell 1981), but the presence of a second invariant may disrupt the similarity. It is possible, however, that J dominates the scaling in the near field, and θ dominates in the far field. This raises the hope that the transverse jet displays intermediate-asymptotic similarity (Barenblatt 1996), which occurs when there are multiple relevant length or time scales in a problem, but the scales are disparate over orders of magnitude. Then, self-similar 'asymptotic' solutions (which strictly hold only when certain scales are infinite or zero) are approximately valid over intermediate length or time scales.

3.1.1. *Assumption of intermediate-asymptotic similarity in the near and far field*

Since the jet has a local characteristic width, $\delta(x_c)$, it can be used to normalize coordinates in the local cross-section. Local Cartesian coordinates, orthogonal to the local trajectory, normalized by δ, are then denoted η and γ. Also ρ, u, and $v - v_\infty$ profiles in the cross-section are normalized by their centreline values, denoted by subscript c:

$$\rho(\eta, \gamma, x_c) = \rho_c(x_c) f(\eta, \gamma; x_c), \tag{3.7}$$

$$u(\eta, \gamma, x_c) = u_c(x_c) g(\eta, \gamma; x_c), \tag{3.8}$$

$$v_\infty - v(\eta, \gamma, x_c) = [v_\infty - v_c(x_c)] h(\eta, \gamma; x_c), \tag{3.9}$$

where the functions f, g and h are normalized profiles in the cross-section. A standard similarity assumption is that these functions are independent of x_c; for the transverse jet, however, experimental data suggest a slightly more sophisticated approach.

Smith & Mungal (1998) define three regions of the flow: (1) a *potential core region*, in the first few diameters from the jet exit (in the Appendix we suggest an analytical means for predicting the length of this region, based on the work of Coelho & Hunt (1989)), (2) a *near-field* region, just beyond the potential core, where the flow is fully turbulent but has not been deflected appreciably, and (3) a *far-field* region where the jet flow has turned almost completely into the crossflow. In the limit of $r \gg 10$, region (1) is similar to an axisymmetric mixing layer, region (2) is similar to a free jet, and region (3) is similar to the wake of a lifting body. Because the terminology is confusing – the transverse jet 'near field' corresponds to the 'far field' of a free jet – we will refer to the near field as the 'jet' region, and the far field as the 'wake' or 'wake-like' region. It is emphasized, however, that 'wake region' does not refer to the region immediately behind the jet, but the main jet flow far from the jet nozzle, where wake-like velocity-deficit scaling is observed.

Based on these observations, it seems appropriate to assume that the profile functions f, g and h become steady in each of these regions, i.e. that their dependence on x_c disappears over an intermediate-asymptotic length scale. This allows for the possibility that the profiles transition from one function in the jet region to another in the wake region.

For example, consider the normalized density profile, $f(\eta, \gamma; x_c) = \rho(\eta, \gamma)/\rho_c(x_c)$. At the jet exit ($x_c = 0$), f nearly has a top-hat profile: $f = 1$ inside the jet, and $f = \rho_\infty/\rho_j$ elsewhere. In the near and far fields, the profile smooths, and eventually relaxes to a uniform profile, where $f \approx 1$ everywhere. In free jets, this evolution occurs quickly – the difference between the centreline and ambient densities decays by a factor of two by the end of the potential core region. In short, taking $\rho_c = \rho_\infty$, $f = 1$ is a reasonable approximation by the time the near field is reached, unless density differences are extreme.

Next consider the normalized u profile, $g(\eta, \gamma; x_c) = u(\eta, \gamma)/u_c(x_c)$. At $x = 0$ (the jet exit), $g = 1$ inside the jet, and $g \approx 0$ elsewhere in the cross-section. In the near field, g approximates a Gaussian distribution. In the far-field, the u profile is complicated, because the flow in the far-field cross-section resembles that of a counter-rotating vortex pair. Fortunately, in the far field, $u_c \to 0$, and u is no longer the dominant velocity component. For now, we need only argue that g asymptotically becomes a self-similar function.

Finally, consider $h = (v_\infty - v)/(v_\infty - v_c)$. At $x = 0$ (the jet exit), the flow can be described approximately as $v = 0$ inside the jet, and $v \approx v_\infty$ elsewhere; therefore h is a 'top-hat' function at the jet exit. In the near field and far field, $h(\eta)$ probably becomes a doubly peaked function, similar to the far-field concentration cross-sections measured by Smith & Mungal (1998).

With these justifications, intermediate-asymptotic similarity is assumed, i.e. that f, g and h asymptotically approach one set of functions (independent of x_c) as $x_c \to 0$, and approach another set of functions (independent of x_c) as $x_c \to \infty$. Furthermore, we assume that the transition from one set of profiles to another is sufficiently rapid that, as a reasonable approximation, we may replace the integrals of the profiles with the limiting constants in each region. With these assumptions, it is now possible to estimate the behaviour of characteristic velocities in the jet (near-field) and wake (far-field) limits.

In the near-field region, where the jet has not been deflected appreciably, the

velocity is dominated by the u-component. Therefore $\sqrt{u^2+v^2} \approx u_c(x)g(\eta,\gamma)$, and the conservation equations (3.4)–(3.6) are simplified in the near field:

$$\dot{m}_j + \dot{m}_\infty = \dot{m} \approx I_{mn}\rho_c u_c \delta^2, \tag{3.10}$$

$$J \approx I_{Jn}\rho_c u_c^2 \delta^2, \tag{3.11}$$

$$\theta \approx I_{\theta n}\rho_c \delta^2 [v_\infty - v_c] u_c. \tag{3.12}$$

In the far-field 'wake' region, where the jet has completed most of the turning, $u \to 0$, $v \to v_\infty$, and the conservation equations (3.4)–(3.6) are again simplified:

$$\dot{m}_j + \dot{m}_\infty = \dot{m} \approx I_{mf}\rho_c v_\infty \delta^2, \tag{3.13}$$

$$J \approx I_{Jf}\rho_c v_\infty u_c \delta^2, \tag{3.14}$$

$$\theta \approx I_{\theta f}\rho_c v_\infty [v_\infty - v_c] \delta^2, \tag{3.15}$$

where the constants I represent the asymptotic values of integrals. The first subscript on the I (namely m, J, θ) corresponds to the integral quantity (i.e. for mass, momentum, or momentum deficit) and the second subscript corresponds to the near- or far-field region of the jet. In the near field,

$$I_{mn} \equiv \int_A fg \,\mathrm{d}\eta \,\mathrm{d}\gamma, \quad I_{Jn} \equiv \int_A fg^2 \,\mathrm{d}\eta \,\mathrm{d}\gamma, \quad I_{\theta n} \equiv \int_A fgh \,\mathrm{d}\eta \,\mathrm{d}\gamma, \tag{3.16}$$

and in the far field,

$$I_{mf} \equiv \int_A f \,\mathrm{d}\eta \,\mathrm{d}\gamma, \quad I_{Jf} \equiv \int_A fg \,\mathrm{d}\eta \,\mathrm{d}\gamma, \quad I_{\theta f} \equiv \int_A fh \,\mathrm{d}\eta \,\mathrm{d}\gamma. \tag{3.17}$$

Profiles measured in previous work (Fric & Roshko 1994; Kuzo 1995) suggest that the integrals vary only by factors of two or so as they evolve from near-field to far-field values. For example, for a Gaussian profile of $g(\eta,\gamma)$, the integral I_{Jn} evaluates to half the value if $g = 1$ across the jet width (keeping mass and momentum flux the same for the profile). This factor of two is small compared with the power-law relationships between u_c, $v_c - v_\infty$ and δ that the conservation equations (3.10)–(3.15) imply.

3.2. *Scaling laws*

3.2.1. *Velocity and jet width: jet region*

If a self-similar (intermediate-asymptotic) jet region exists, J is the defining invariant and v_∞ is unimportant. From dimensional analysis, the functional dependence $u_c = \phi(J, x, \rho_\infty, v)$ becomes $\Pi = \Phi(\Pi_1)$, where

$$\Pi = \frac{\rho_\infty^{1/2} u_c x}{J^{1/2}} \sim \frac{u_c}{u_j}\frac{x}{d*}, \tag{3.18}$$

$$\Pi_1 = \frac{J^{1/2}}{\rho_\infty^{1/2} v} = Re, \tag{3.19}$$

and $d* = d_j(\rho_j/\rho_\infty)^{1/2}$. If we invoke Reynolds number (Re) invariance, the functional dependence reduces to Π = constant (some Re dependence is suggested by Yuan, Street & Ferziger (1999); we are assuming a much stronger dependence on r). We have also observed that J is constant, and hence have two equations for two unknowns

(u_c and δ). Substituting for u_c with the above expression for Π, into (3.11), letting $\rho_c \to \rho_\infty$, gives

$$J = I_{Jn}\rho_c \Pi^2 d^{*2} u_j^2 \left(\frac{\delta}{x}\right)^2. \tag{3.20}$$

Since everything in this equation is a known constant for a given jet save δ/x, δ/x must also be a constant. Therefore,

$$\delta \sim x, \tag{3.21}$$

$$u_c \sim J^{1/2}\rho_\infty^{-1/2}x^{-1}. \tag{3.22}$$

These results agree with free-jet scaling, as expected. The dependence of v_c on x is derived by considering the momentum deficit in the near field, (3.12). The relationship is

$$v_\infty - v_c \sim \frac{\theta}{\rho_\infty^{1/2} J^{1/2}} x^{-1}. \tag{3.23}$$

3.2.2. *Velocity and jet width: wake-like region*

In the wake-like region, the characteristic velocity deficit $v_\infty - v_c$ is of interest. Adding v_∞ to the parameter list, the functional dependence is $v_\infty - v_c = \phi(J, x, \rho_\infty, \nu, v_\infty)$. Dimensional analysis gives $\Pi = \Phi(\Pi_1, \Pi_2)$ where

$$\Pi = \frac{v_\infty - v_c}{v_\infty}, \tag{3.24}$$

$$\Pi_1 = \frac{x\rho_\infty^{1/2} v_\infty}{J^{1/2}} \sim \frac{x}{rd}, \tag{3.25}$$

$$\Pi_2 = \frac{J^{1/2}}{\rho_\infty^{1/2}\nu} = Re. \tag{3.26}$$

This time, the assumption of Reynolds number invariance leads to $\Pi = \Phi(\Pi_1)$. From (3.15), letting $\rho_c \to \rho_\infty$ and $v_c \to v_\infty$, we obtain

$$\theta = I_{\theta f}\rho_c v_\infty (v_\infty - v_c)\delta^2 = I_{\theta f} J \Pi \Pi_1^2 \frac{\delta^2}{x^2}. \tag{3.27}$$

At this point it is necessary to make an assumption: that δ/x and the product $\Pi\Pi_1^2$ are constants. The assumption is motivated by the scaling of three-dimensional wakes (Cantwell 1981), but requires experimental verification. In the meantime, this assumption leads to scaling laws for characteristic length and velocity deficit:

$$\delta \sim x, \tag{3.28}$$

$$v_\infty - v_c \sim \frac{J}{\rho_\infty v_\infty} x^{-2}. \tag{3.29}$$

Using (3.14) and substituting for δ, and absorbing the integral into a constant, gives

$$u_c(x) \sim \frac{J}{\rho_\infty v_\infty} x^{-2}. \tag{3.30}$$

If the data indeed verify that $\delta/x =$ constant in both the far field and near field, it would indicate a sort of degeneracy in the similarity. However, it is emphasized that the constants could be different in the near and far fields as a consequence of different normalized velocity profiles (resulting from different flow structure), as described previously.

3.2.3. *Mass flux*

The scaling laws for velocity and jet width can be used to derive near- and far-field scaling laws for mass flux, so that constants of proportionality can be combined into a near- and far-field entrainment coefficient. This will also allow comparison with experimental measurements, and an easy way to check for consistency between the coefficients for scalar/velocity and the observed profiles.

In the near field, $\dot{m} \sim \rho_c u_c \delta^2$; substituting the near-field scaling laws (3.21) and (3.22) for δ and u_c, and assuming $\rho_c \approx \rho_\infty$, leads to $\dot{m}(x) \sim \rho_\infty^{1/2} J^{1/2} x$. (The assumption that $\rho_c \approx \rho_\infty$, of course, is not very good until at least 10 diameters from the jet nozzle, depending on the density ratio; however, we are restricting ourselves to the region $x/d > 10$ for similarity purposes anyway.) If the flow from the jet exit is perfectly uniform, $J = \dot{m}_j u_j$, and $\dot{m}_j = \rho_j u_j \frac{1}{4}\pi d^2$, so

$$\frac{\dot{m}(x)}{\dot{m}_j} = c_{ej} \left(\frac{\rho_\infty}{\rho_j}\right)^{1/2} \left(\frac{x}{d}\right), \tag{3.31}$$

where c_{ej} is the entrainment coefficient. The subscript e is used to denote entrainment, and the subscript j is used to denote that the coefficient holds in the jet (near-field) region of the flow. Equation (3.31) was confirmed by Ricou & Spalding (1961) for free jets, with $c_{ej} = 0.32$.

In the far field, $u_c \to 0$ and $v_c \to v_\infty$, hence the mass flux becomes $\dot{m}(x) \sim \rho_c v_c \delta^2 \sim \rho_\infty v_\infty x^2$. Assuming an ideal jet exit velocity profile as before, the scaling law for δ gives

$$\frac{\dot{m}(x)}{\dot{m}_j} = c_{ew} r \left(\frac{\rho_\infty}{\rho_j}\right)^{1/2} \left(\frac{x}{rd}\right)^2, \tag{3.32}$$

where c_{ew} is the entrainment coefficient in the wake-like region. Comparison of near- and far-field entrainment rates leads to a definition of a dividing line between jet and wake flow regimes. The jet entrainment law (3.31) predicts more rapid entrainment than the wake-like entrainment law (3.32) until $x/rd = c_{ej}/c_{ew}$, suggesting that the transition point from jet to wake-like behaviour should be at a critical value of x/rd. In § 4.1, using scalar concentration data, we will demonstrate that this type of scaling transition indeed occurs for jets with $r \geqslant 20$.

Returning to the reduced balance equations (3.10)–(3.15), scaling laws for the centreline velocities can be written in terms of the entrainment coefficients, if we also introduce profile factors which relate the centreline values to the mass-flux averaged values. Under the ideal nozzle flow assumption, $J = \dot{m}_j u_j$ and $\theta = \dot{m}_j v_\infty$; therefore

$$\frac{u_c}{u_j} = c_u \frac{\dot{m}_j}{\dot{m}}, \quad \frac{v_\infty - v_c}{v_\infty} = c_v \frac{\dot{m}_j}{\dot{m}}, \tag{3.33}$$

where c_u and c_v are profile coefficients. Again, it is emphasized that these may have different asymptotic values in the near and far fields, because of the differences in asymptotic profiles f, g and h in these regions.

3.2.4. *Trajectory*

Based on these scaling laws, simple analytic solutions can be obtained for the trajectory in the jet and wake-like regions. The trajectory can be defined as the mean centre streamline, such that $\mathrm{d}x/\mathrm{d}y = u_c/v_c$. Equations (3.22) and (3.30) provide u_c in the near and far fields, respectively, and it is assumed that $v \to v_\infty$. Ignoring the profile coefficients (assuming that the mass-flux averaged velocities, not the peak velocities,

determine the trajectory), gives the trajectories

$$\frac{x_c}{rd} = \left(\frac{2}{c_{ej}}\frac{y_c}{rd}\right)^{1/2}, \tag{3.34}$$

$$\frac{x_c}{rd} = \left(\frac{3}{c_{ew}}\frac{y_c}{rd}\right)^{1/3} \tag{3.35}$$

for the jet and wake-like regions, respectively. From these equations it is clear that the entrainment coefficient is directly related to the jet trajectory. In other words, neglecting pressure forces on the jet (they are $O(r^{-2})$ compared to momentum flux terms), implies that the jet is deflected entirely due to entrainment of crossflow fluid. Therefore, the rate of entrainment can be deduced from the rate of turning. This semi-empirical approach was successfully applied to predicting scalar concentration and velocity in previous work (Hasselbrink & Mungal 1996), but the results were limited to the far field.

The form of the far-field trajectory (3.35) was found by Margason (1968), as $x/rd = 1.6(y/rd)^{1/3}$. A very close approximation to this was also found by Pratte & Baines (1967): $x/rd = 2.05(y/rd)^{0.28}$. In general, experimental results show significant scatter, particularly in the leading coefficient, as shown in the trajectory data compiled by Margason (1993). As discussed in the introduction, this is due to at least five effects:

(i) the trajectories of maximum flow speed, maximum scalar concentration, and the centre streamline are different (Kamotani & Greber 1972);

(ii) approximations inherent in flow visualization;

(iii) different forms of assumed trajectory correlations;

(iv) different ranges of r which were correlated (we expect a correlation of the form given in (3.35) only for $r \gg 1$);

(v) differing methods for calculating r, such as using the average or peak velocity at the jet exit rather than the momentum average.

Margason's values are used in the remaining discussion, i.e. $c_{ew} = 0.73$. With the trajectory given in (3.35), and again assuming ideal flow from the nozzle, the mass flux in the far field can also be written in terms of y/rd, the more natural far-field spatial variable:

$$\frac{\dot{m}}{\dot{m}_j} = (9c_{ew})^{1/3} r \left(\frac{\rho_\infty}{\rho_j}\right)^{1/2} \left(\frac{y}{rd}\right)^{2/3}. \tag{3.36}$$

This result is exactly the form obtained by Broadwell & Breidenthal (1984).

3.2.5. *Scalar concentration*

A scaling law for concentration can be derived by considering the conservation of scalar. Presuming normalized concentration, ξ, is unity at the jet exit and zero in the crossflow, the conservation equation is

$$\dot{m}_j = \int_{A_s} \rho(u^2 + v^2)^{1/2} \xi \, \mathrm{d}A_s. \tag{3.37}$$

By simplifying the integral to a normalized profile, and making the same near-field and far-field simplifications as in previous sections, the equation can be reduced to

$$\xi_c = c_\xi \frac{\dot{m}_j}{\dot{m}}, \tag{3.38}$$

where ξ_c denotes the centreline concentration, and c_ξ is a profile shape factor. Using the near- and far-field scaling laws for mass entrainment,

$$\xi_c = \frac{c_\xi}{c_{ej}} \left(\frac{\rho_\infty}{\rho_j}\right)^{1/2} \left(\frac{x}{d}\right)^{-1}, \tag{3.39}$$

in the near field. Note that $c_\xi = 1.6$ in free jets, since $c_\xi/c_{ej} = 5.0$, and $c_{ej} = 0.32$ (Chen & Rodi 1980). In the far field,

$$\xi_c = \frac{c_\xi}{c_{ew}} \frac{1}{r} \left(\frac{\rho_j}{\rho_\infty}\right)^{1/2} \left(\frac{x}{rd}\right)^{-2} = \frac{c_\xi}{(9c_{ew})^{1/3}} \frac{1}{r} \left(\frac{\rho_j}{\rho_\infty}\right)^{1/2} \left(\frac{y}{rd}\right)^{-2/3}. \tag{3.40}$$

Assuming that c_ξ is still 1.6, the leading coefficient evaluates to 0.85. Because profiles are expected to change as the asymptotic profiles change, this is not necessarily a good assumption; however, the experimental data will show that this gives fortuitously accurate results.

3.3. *Scaling law summary*

The scaling laws can be condensed by employing near- and far-field entrainment coefficients, c_{ej} and c_{ew}, and profile factors which relate centreline values to flux-averaged values. Assuming a uniform jet-exit profile also allows J and θ to be replaced by the more intuitive quantities of jet exit velocity and jet diameter. In the near field, in terms of x_c:

$$\frac{u_c}{u_j} = \frac{c_{uj}}{c_{ej}} \left(\frac{\rho_j}{\rho_\infty}\right)^{1/2} \left(\frac{x_c}{d}\right)^{-1}, \tag{3.41}$$

$$\frac{v_\infty - v_c}{v_\infty} = \frac{c_{vj}}{c_{ej}} \left(\frac{\rho_j}{\rho_\infty}\right)^{1/2} \left(\frac{x_c}{d}\right)^{-1}, \tag{3.42}$$

$$\xi_c = \frac{c_\xi}{c_{ej}} \left(\frac{\rho_\infty}{\rho_j}\right)^{1/2} \left(\frac{x_c}{d}\right)^{-1}. \tag{3.43}$$

In the far field, making use of y/rd as the preferred distance metric:

$$\frac{u_c}{u_j} = \frac{c_{uw}}{(9c_{ew})^{1/3}} \frac{1}{r} \left(\frac{\rho_j}{\rho_\infty}\right)^{1/2} \left(\frac{y_c}{rd}\right)^{-2/3}, \tag{3.44}$$

$$\frac{v_\infty - v_c}{v_\infty} = \frac{c_{vw}}{(9c_{ew})^{1/3}} \frac{1}{r} \left(\frac{\rho_j}{\rho_\infty}\right)^{1/2} \left(\frac{y_c}{rd}\right)^{-2/3}, \tag{3.45}$$

$$\xi_c = \frac{c_\xi}{(9c_{ew})^{1/3}} \frac{1}{r} \left(\frac{\rho_j}{\rho_\infty}\right)^{1/2} \left(\frac{y_c}{rd}\right)^{-2/3}. \tag{3.46}$$

In each region the scaling laws are the same except for the leading constants, which arise from profile differences. The subscripts on the profile constants refer to the quantity (u, v, or ξ) and the region of the jet (near or far field), respectively.

Approximate values for many of the profile constants can be estimated. In free jets, the leading constant in the scaling law given by (3.41) is 6.2 (Chen & Rodi 1980); since $c_{ej} = 0.32$ (Ricou & Spalding 1961), it follows that $c_{uj} \approx 2$. This value can also be derived by comparing the centreline velocities of a top-hat profile with a Gaussian profile, and assuming they have the same mass and momentum flux. Similar values of c_{vw} and c_{uw} are expected, since these are peaked profiles; c_{vj}, however, should reflect

the relatively flat profiles of v in the near field, and should therefore be near unity. Other coefficients can be deduced from data. As will be shown in the following section, the far-field entrainment coefficient $c_{ew} \approx 0.73$, although uncertainty in this number is somewhat large, because it is based on indirect measures such as jet trajectory and centreline velocity. The scalar profile coefficient $c_\xi \approx 1.6$ in both the near and far fields.

4. Comparison to data

4.1. *Scalar concentration*

For comparison to scalar concentration data, we have revisited the data of Smith & Mungal (1998), who have performed an exhaustive set of concentration measurements. Their experiments measured the concentration field in various planes through a nearly constant-density transverse jet at $r = 5$, 10, 15, 20 and 25 using planar laser-induced fluorescence (PLIF) of acetone. They also acquired a small set of concentration images at $r = 40$, 80 and 200. The jet issues from contoured nozzles of various diameters, flush with the wall of a 50×50 cm wind tunnel with uniform crossflow velocity of $1.25\,\mathrm{m\,s^{-1}}$. A 300 μm thick sheet of laser light is used to induce fluorescence of acetone vapour, initially at about 10% concentration in the jet. The fluorescence signal, captured on a cooled 512×512 pixel CCD camera, is linearly proportional to the acetone concentration, after correction for laser sheet intensity distribution, background signal, and the absorption of laser energy by the acetone. Further experimental details are given in Smith (1996) and Smith & Mungal (1998).

4.1.1. *Scalar: jet region*

Ensemble averages of instantaneous concentration fields of three jets with $r = 40$, 80, and 200 are shown on figure 3(*a*). Crossflow is from bottom to top, and the jet issues from left to right with jet exit Reynolds numbers of 8300, 17 000 and 33 000, respectively. Nozzle diameters are 2.5, 2.5 and 2.0 mm, respectively, and the viewing region is approximately 230 mm tall by 250 mm wide. These images were obtained as an adjunct experiment to more exhaustive imaging at lower r, and so the laser sheet and camera positions were kept fixed, despite sub-optimal windowing at these values of r. Only 10–20 images were acquired for the ensemble average, yet the smoothness of the profiles suggests converged mean values; this is probably a result of spatial averaging in each pixel.

The data clearly show a free-jet scaling region in the transverse jet. First of all, in all three cases there is a region near the nozzle where the jet appears to spread linearly, although the overall jet is also slightly deflected. Note that a logarithmic look-up table has been employed for the image display, which accentuates regions of low concentration, and overemphasizes the skewness and distortion in the concentration profile. Concentration profiles (taken through vertical slices through the images) are shown on figure 3(*b*) for each case. The vertical distance is normalized by the horizontal distance from the nozzle, and scalar concentration is normalized by x/d. Without crossflow, the profiles would collapse to a single curve in this coordinate system; this is closely realized for all the data in the $r = 200$ case, except for some horizontal shifting of the profiles. Figure 3(*c*) shows improvement in data collapse, afforded by shifting the profiles by the jet centreline displacement in y, predicted by the near-field trajectory (equation (3.34) gives $y_c/x_c = 0.16x_c/rd$). The collapse of the $r = 200$ data is good for all available data (as far as 72 diameters from the nozzle exit). In the $r = 80$ case, noticeable disagreement in the scaling for the peak value

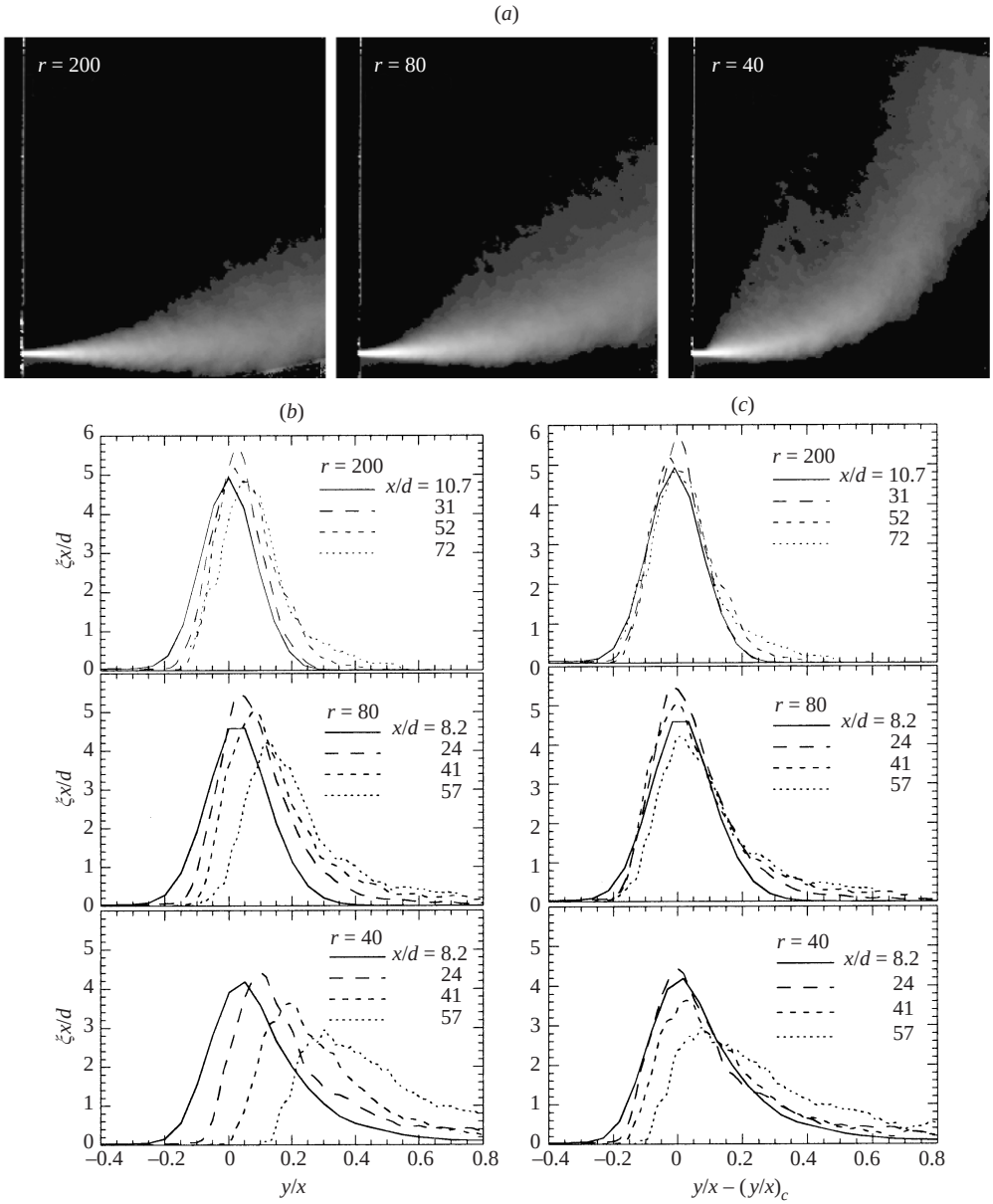

FIGURE 3. Jet-like behaviour in the concentration field of transverse jets. (*a*) Average concentration images at $r = 200$, $r = 80$, $r = 40$, data from Smith (1996). (*b*) Concentration profiles taken along vertical cuts through the images, cast into jet-similarity coordinates. (*c*) Concentration profiles, shifted horizontally in order to centre profiles onto the location of jet centreline. Centreline is predicted by the near-field trajectory $x_c/rd = (2/c_{ej})^{1/2}(y_c/rd)^{1/2}$; with $c_{ej} = 0.32$, the shift is $y_c/x_c = 0.16x/rd$. Free-jet profiles would collapse to a single Gaussian-like curve with maximum value near 5.0. In the transverse jet, although the profiles translate in the crossflow direction, they stay relatively symmetric and the maximum stays near 5.0 for all data in the $r = 200$ case, for $r = 80$ when $x/d < 40$, and for $r = 40$ when $x/d < 20$.

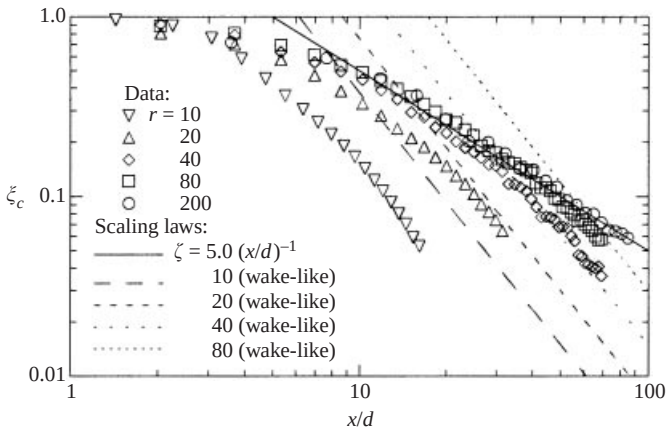

FIGURE 4. Centreline scalar concentration transition from jet-like to wake-like behaviour. At $r > 20$, a region exists in the near field where the free-jet scaling law is obeyed. At a point near $x_c/d = (3/4)r$, a transition to a wake-like scaling law, equation (3.40), is obeyed.

of ξ does not occur until $x/d > 40$; in the $r = 40$ case, the peak value obeys the jet scaling law until $x/d > 33$.

Another test for jet similarity is the scaling of the centreline concentration decay. Figure 4 shows peak concentration as a function of vertical distance from the jet nozzle for all three cases, plus additional data for the $r = 10$ and $r = 20$ cases. The data are compared with the expression given by Chen & Rodi (1980) for free jets, $\xi = 5(x/d)^{-1}$. The data for $r = 40$, 80 and 200 show good agreement until $x/d \approx (3/4)r$. It thus appears that for high-r jets, free-jet scaling applies over an intermediate length scale. Based on the analysis and the experimental data shown above, it appears that this length scale is defined as $x/rd < 3/4$. This region also has a lower bound, because jet similarity is not expected until $x/d > 10$, well away from the potential core. Therefore the jet-like intermediate region is not expected to appear unless $r > 20$.

4.1.2. *Scalar: wake-like region*

Figure 4 also shows the predicted concentrations using the scaling law in the wake-like region, equation (3.40) with $c_{ew} = 0.73$, and $c_\xi = 1.6$. The agreement appears to be very good, except for the $r = 10$ case, but recall that the analysis assumed $r \gg 1$. These data suggest that $r > 20$ is required for a jet scaling region to appear in the concentration field.

However, the scaling laws appear to work somewhat better for $r < 20$ jets in the far field. Figure 5 compares the scaling law in y/rd coordinates to the results of Smith & Mungal (1998) at $r = 5$, 10, 15, 20 and 25. The worst deviation is for $r = 10$, which has an anomalous dip in the centreline concentration data near $y/rd = 1.7$, where the concentration falls 31% below the predicted value. However, images from Smith & Mungal (1998) show that centreline concentration in the far field can be 40% less than the peak value, which is found off-centreline, in the CVP cores. The present theory makes no attempt to account for details of the concentration distribution in the cross-section. However, the collapse of the data suggests that concentration is properly scaled with r – in the far field for $r \geqslant 10$ and $y/rd > 2$, deviation is under 22%.

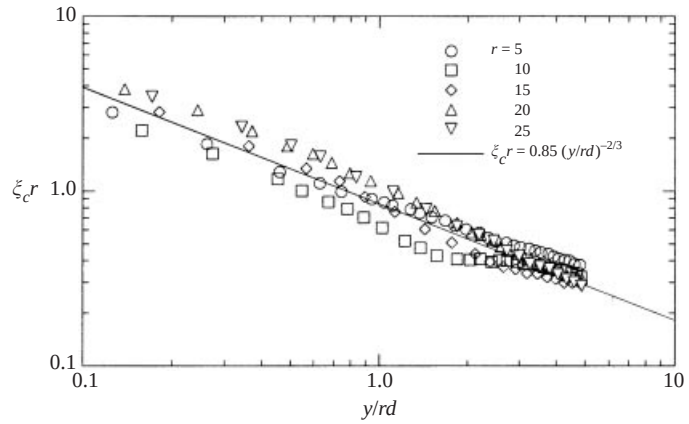

FIGURE 5. Scalar concentration collapsed with r, versus y/rd, compared with far-field (wake-like) scaling law. Data are from Smith & Mungal (1998).

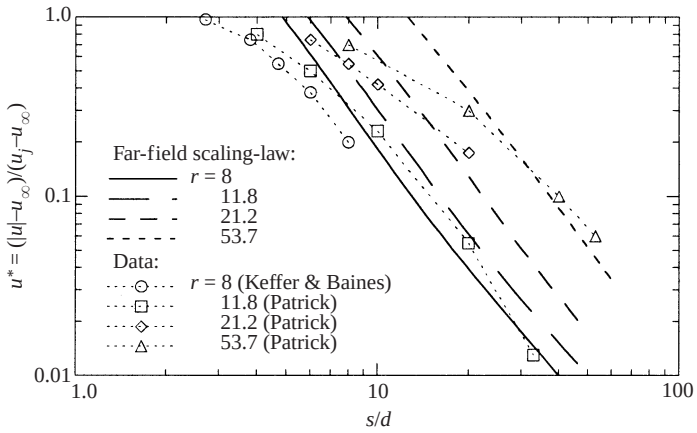

FIGURE 6. Comparison of existing high-r velocity data with calculations from far-field scaling laws.

4.2. *Velocity*

Figure 6 compares the centreline velocity magnitude prediction of the analysis with velocity data obtained from Patrick (1967) and Keffer & Baines (1963). The data from these experiments were originally plotted as a function of s/d, so we calculate s by numerically integrating:

$$s = \int_0^s \mathrm{d}s = \int_0^x \left[\left(\frac{\mathrm{d}x^2}{\mathrm{d}y^2}\right) + 1\right]^{1/2} \mathrm{d}y, \tag{4.1}$$

where the trajectory is as given in (3.35). Also, Patrick's velocity data were normalized as $u^* = (|\boldsymbol{u}_c| - v_\infty)/(u_j - v_\infty)$.

Due to the generally sparse velocity data in the literature for high-r jets, an extensive set of particle image velocimetry (PIV) data were obtained in our laboratory for $r = 10$ and $r = 20$. We defer more complete description of the experiment until Part 2 of this paper (Hasselbrink & Mungal 2001), but for the purposes of validating the scaling laws given here, we present the results in figure 7. The plots compare profiles (obtained in the (x, y)-plane through the centre of the jet) of mean v velocity (top) and RMS

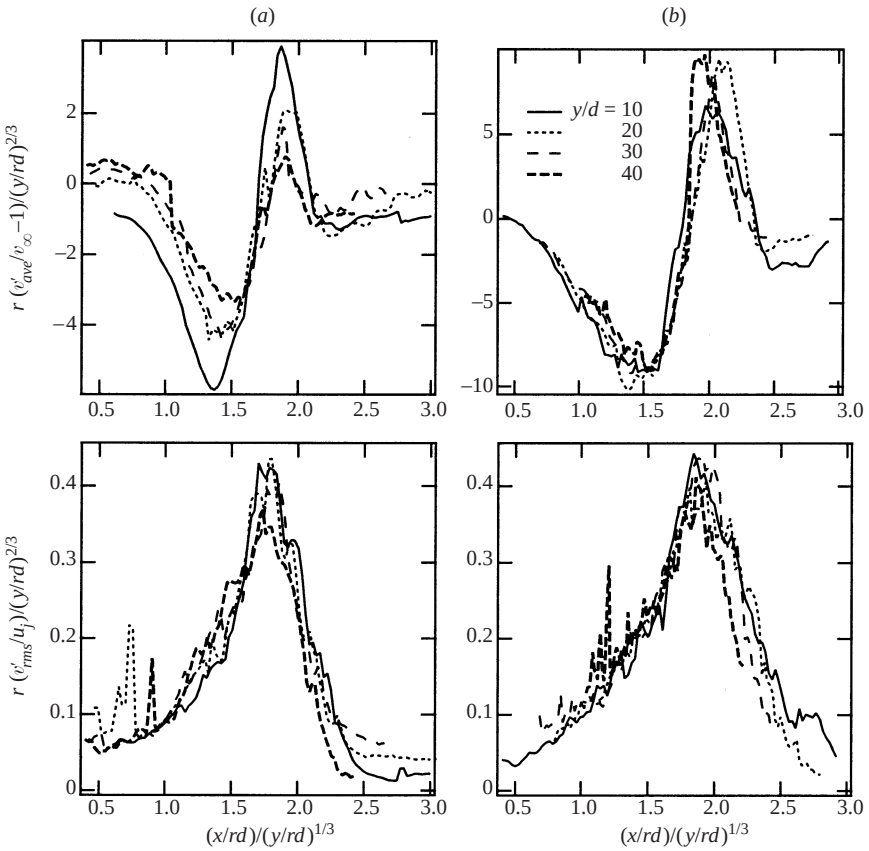

FIGURE 7. Jet cases: velocity (top) and RMS fluctuation (bottom) profiles in far-field similarity coordinates. (*a*) $r = 10$ jet, (*b*) $r = 21$ jet.

fluctuations (bottom), for $r = 10$ (*a*) and $r = 21$ (*b*) jets, in similarity coordinates. The spatial coordinate x/rd has been scaled by $(y/rd)^{1/3}$, as suggested by equation (3.35). The mean and RMS velocity profiles (top) have been scaled as suggested by equation (3.45) (the scaling of v'_{rms} by u_j in the RMS profiles is not necessarily obvious, but is discussed in Part 2). As found in the concentration data, self-similar collapse is less perfect for $r = 10$ as suggested in § 3; however, the collapse of the data is good for $r = 21$ for both the mean and RMS profiles.

5. Implications for the counter-rotating vortex pair

5.1. *Vorticity in the vortex pair*

The structure of the far-field vorticity field is often depicted as a counter-rotating vortex pair (CVP) with compact cores, as shown in figure 1. This concept of the CVP, where the vorticity is aligned with the jet axis, is based on the appearance of a vortex-pair-like distribution of mean vorticity, velocity, and scalar in the jet cross-section. However, a different picture evolves from the consideration of fundamental equations of motion, coupled with the scaling laws.

From Batchelor (1967, equation 7.2.5), a body of fluid has linear momentum, $\boldsymbol{P}$,

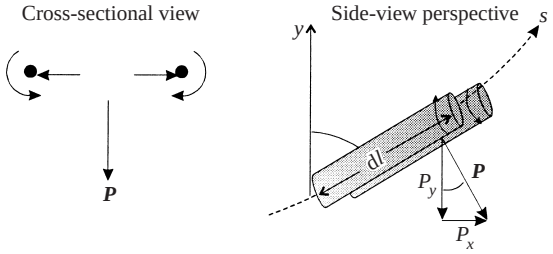

FIGURE 8. Schematic of CVP model.

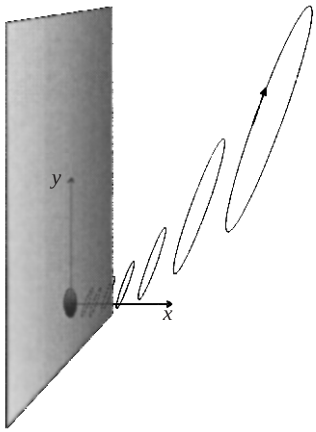

FIGURE 9. Vorticity field structure implied by the CVP model.

which is proportional to the first moment of the vorticity field, $\boldsymbol{\omega}$:

$$\boldsymbol{P} = \tfrac{1}{2}\rho \int_V \boldsymbol{x} \times \boldsymbol{\omega}\, \mathrm{d}V, \tag{5.1}$$

where $\boldsymbol{x}$ is a position vector.

If the CVP is idealized as a pair of potential vortices, the CVP is completely defined by its circulation Γ and spacing δ_{cvp}, as shown in figure 8. Equation (5.1) simplifies to (Batchelor 1967)

$$\mathrm{d}\boldsymbol{P} = \rho \Gamma\, \delta_{cvp}\, \mathrm{d}l \hat{\boldsymbol{n}} \tag{5.2}$$

where $\mathrm{d}l$ is a differential distance along the vortex line, and $\hat{\boldsymbol{n}}$ is a unit vector in the direction of propagation. In the transverse jet, this vortex impulse arises from the momentum excess in the x-direction and deficit in the y-direction. In a time $\mathrm{d}t$, a differential amount of x-momentum and y-momentum deficit are released from the jet exit (again neglecting pressure effects, requiring $r \gg 1$):

$$\mathrm{d}P_x = \dot{m}_j u_j\, \mathrm{d}t, \tag{5.3}$$

$$\mathrm{d}P_y = \dot{m}_j v_\infty\, \mathrm{d}t. \tag{5.4}$$

Therefore $\mathrm{d}P_x/\mathrm{d}P_y = u_j/v_\infty$ is constant, and hence the impulse vector $\boldsymbol{P}$ has a constant angle of inclination to the crossflow throughout the jet trajectory. This leads to a surprising conclusion: *the idealized vortex pair has a constant angle of inclination throughout the jet:* $\alpha_{cvp} = \arctan(v_\infty/u_j)$.

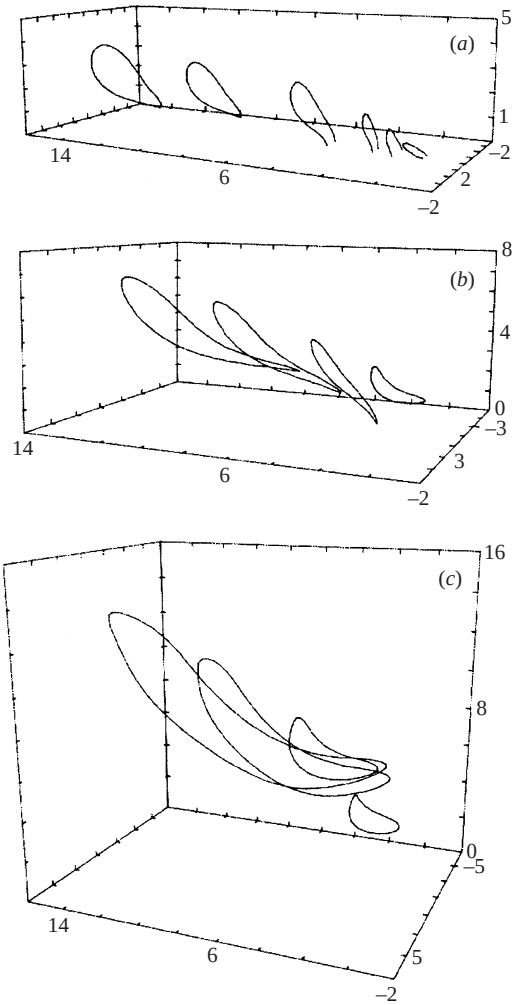

FIGURE 10. Vortex lines in the transverse jet, from Sykes *et al.* (1986). Crossflow is from right to left (axes are rotated 90° clockwise from the present work). (*a*)–(*c*), $r = 2$, 4 and 8. Jet exit centre is at (0,0,0) in the coordinate system shown, and axes are normalized by jet diameter. Reprinted with permission from Cambridge University Press.

The structure of the vorticity field implied by this finding is incompatible with the conventional concept of the CVP vortex lines being parallel with the jet trajectory (figure 1). A simplified conceptual view that is consistent with this result is presented in figure 9, which also attempts to account for the fact that vortex lines cannot terminate within the fluid. This structure is radically different from the typical portrayal of the CVP in the literature. Of course, this structure is correct only to leading order: the layered structure shown implies that vorticity must be distributed throughout each cross-section, which is inconsistent with the assumption of compact vorticity (e.g. an ideal vortex pair). Furthermore, this analysis only considers the time-average field. Experimental work by Kelso *et al.* (1996) and simulations by Yuan *et al.* (1999) indicates that the instantaneous vorticity field structure is significantly more complicated, involving bent and distorted vortex 'rings' which interconnect with each other.

The computational results of Sykes *et al.* (1986) demonstrate a more realistic structure which is consistent with this analysis, shown in their figure 12, reproduced in figure 10. In their simulation (crossflow goes right to left, jet initially issuing upwards), vortex lines form slightly curved rings starting at the front of the jet which incline into the crosswind. As the rings move upwards, they also stretch downstream, becoming elongated. However, rings within a single jet all have a similar inclination angle to the crossflow (except, perhaps, very close to the nozzle). For their $r = 2$ case, these rings are inclined at approximately 30° in the far field, as expected, and about half as much for $r = 4$. At $r = 8$, the rings stay almost totally flat as they advect into the crossflow stream. The predictions are also consistent with the experiment of Chang & Vakili (1995), who injected single vortex rings into a crossflow and found that the rings tilted towards the crosswind in this manner. They also found that rings formed at lower nozzle velocities tilted more into the crosswind. Finally, flow visualization of forced jets at moderate *Re* (Eroglu & Breidenthal 1991) clearly shows vortex rings which tilt into the crosswind, rather than away from it. These and other experiments (Kelso *et al.* 1996) suggest that individual vortex rings do not simply tilt as though they were solid disks, but that their leading edges are bent slightly towards the wall, and their trailing edges are bent away from it. As this evolves, the trailing edge of one ring can be entrained upwards into its predecessor.

5.2. *Circulation*

The measured rate of circulation loss in the CVP has previously been attributed to viscous diffusion, which is greatly amplified by turbulent transport and the generation of large vorticity gradients. However, in our proposed strucure of the mean vorticity field in the time-averaged transverse jet, the measured circulation in the half-plane does not correspond to a single vortex tube. Rather, the half-plane circulation is measured across an ensemble of vortex lines, which changes depending on the measurement plane chosen. Therefore, measured circulation is not conserved in the inviscid limit, and its rate of decay is not necessarily due to the rate of vorticity dissipation by turbulent transport.

Nonetheless, the half-plane cross-section circulation has been measured in previous work. Likewise, a scaling law for circulation can be derived from the previous considerations. The x-component of vortex impulse flux is equal to the jet momentum flux:

$$\frac{\mathrm{d}P_x}{\mathrm{d}t} = \frac{\mathrm{d}P}{\mathrm{d}l}\cos(\alpha)\frac{\mathrm{d}l}{\mathrm{d}s}\frac{\mathrm{d}s}{\mathrm{d}t} = J; \tag{5.5}$$

$\mathrm{d}P/\mathrm{d}l$ can be obtained from (5.2), and $\mathrm{d}s/\mathrm{d}t = |u|$. In the far field, $v \to v_\infty$, and $\mathrm{d}l/\mathrm{d}s \to 1/\cos(\alpha)$. Making these substitutions, taking $\rho \to \rho_\infty$, and assuming ideal flow at the nozzle exit ($J = u_j^2 d^2 \pi/4$) gives

$$\frac{\Gamma}{u_j d}\frac{\delta_{cvp}}{rd} = \frac{\pi}{4}\left(\frac{\rho_j}{\rho_\infty}\right)^{1/2}. \tag{5.6}$$

The similarity analysis for the entrainment, presented earlier, implies that $\delta_{cvp} \sim x$. Kuzo (1995) has recently obtained PIV vector fields in the cross-section of the CVP, from eleven contour maps for $r = 5$, 10 and 20 (his figure 20), we have measured the distance between vorticity peaks to be between $0.37x$ and $0.43x$. Taking $\delta = 0.4x$, we have $\delta_{cvp}/rd = 0.4x/rd$. Since Kuzo's circulation data are plotted versus y/rd, we transform coordinates using the far-field trajectory $x/rd = 1.6(y/rd)^{1/3}$, finally

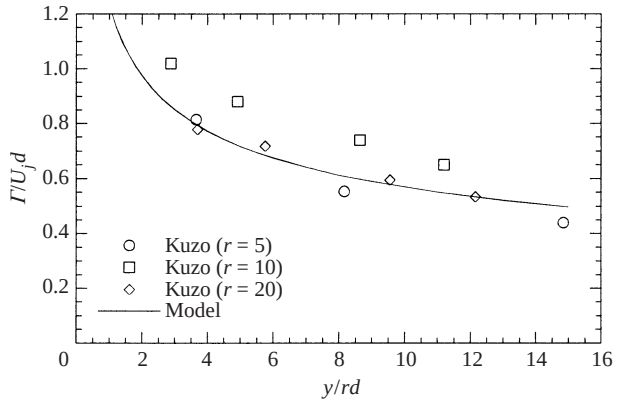

FIGURE 11. CVP circulation versus y/rd; data of Kuzo (1995), compared with model predictions.

arriving at a circulation prediction for the far field:

$$\frac{\Gamma}{u_j d} = \frac{\pi}{2.56}\left(\frac{\rho_j}{\rho_\infty}\right)^{1/2}\left(\frac{y}{rd}\right)^{-1/3}. \tag{5.7}$$

Presented in figure 11 is the predicted vortex circulation compared with Kuzo's results for $r = 5$, 10 and 20 as functions of y/rd. The agreement is quite good, considering the approximations involved. It should also be noted that the scalings $\Gamma/u_j d$ and x/rd collapse the data reasonably well. The quantitative agreement achieved here is quite similar to that obtained by Karagozian (1986), although the present work takes a considerably different approach. The results also agree with the predictions of Durando (1971) and Broadwell & Breidenthal (1984) that $\Gamma \sim y^{-1/3}$.

It is emphasized again that this rate of decay of circulation is not necessarily due to turbulent transport followed by viscous destruction of vorticity, because the measured circulation is not circulation within a single vortex tube. The decay of measured circulation may also result from the spatial integral being taken across a decreasing number of time-averaged vortices.

6. Conclusions

The virtue of similarity analysis is its simplicity. With the entrainment given by equations (3.31) and (3.36), back-of-the-envelope estimation and scaling are possible for far-field transverse jet mean properties.

Besides the simplicity of these scaling laws, there are two particularly interesting results of the analytical work. First of all, in both near and far fields, $\delta \sim x$ (although the proportionality constant may be different in these two regions). The resulting trajectory, $x/rd \sim (y/rd)^{1/3}$, implies that $\delta \sim y^{1/3}$, which is the classical scaling for axisymmetric wakes. Secondly, the equivalence of the 'vortex pair' impulse and the first moment of vorticity directly implies that average vorticity is aligned at a constant angle of inclination to the crossflow. This leads to a vorticity field structure which is quite different from what has typically been assumed in previous modelling efforts.

Various effects have been neglected in the present analysis, which should be included before using the scaling laws for direct engineering application. First of all, we have assumed that pressure terms in the momentum conservation equation are negligible, equivalently that $r^2 \gg 1$. Sensitivity of the entrainment estimate to this neglected

effect leads to noticeable but not overwhelming errors. For example, if kept in the analysis, the pressure term affects the value of the leading coefficient for the trajectory by a factor $(1 - c_L/r^2)^{1/3}$. Given our estimate that $c_L = 10$, we expect the trajectory to be about 25% lower for $r = 5$ than for large r, in rd coordinates; in fact, this behaviour has been observed in the data of Smith & Mungal (1998). Secondly, in the case of jets issuing from a wall, 'image' vortices would be expected to lower the trajectory due to their induced velocity. Again, this effect is expected to be most noticeable at low r. We have refrained from attempting to include these effects, first because similarity in the equations requires the elimination of pressure terms, and secondly, for the sake of clarity. Other confusing factors, such as the virtual origin of the jet, interaction between the jet and the boundary layer, and detailed velocity profile considerations, have likewise been neglected.

Neglecting the crossflow in the near field may seem ignorant in the light of the complicated streamline patterns observed around the jet near field by previous investigators (Coelho & Hunt 1989; Fric & Roshko 1994; Kelso *et al.* 1996). However, the complex streamline patterns noted previously take place in regions where velocity magnitudes are comparatively low. The present approach demonstrates that, for small x/rd, the axial jet velocity is r times larger, and is changing r times faster, than the crossflow component of velocity. Hence the crossflow component can be ignored in this region of the flow.

Remaining issues to be discussed in Part 2 of this paper regarding transverse jet scaling laws include:

(*a*) verification of the near-field/far-field scaling behaviour in the velocity field;

(*b*) investigation of the scaling of turbulence statistics;

(*c*) extending the scaling laws to the case of momentum-dominated diffusion flames.

On this last topic, we are motivated by the results of Gollahallii, Brzustowski & Sullivan (1975), who studied a non-buoyant high-Re propane diffusion flame in a crossflow. Their trajectory data show good agreement to $x/rd = 1.8(y/rd)^{1/3}$. This result is close enough to the present results that it seems possible to extend the analysis to burning jets by using additional conservation laws.

7. A closing remark

Similarity solutions have been classified by Barenblatt & Zel'dovich (1972) and Barenblatt (1996). They state that for a functional dependence $\Pi = \Phi(\Pi_1, \Pi_2)$, there are three possibilities:

(*a*) As $\Pi_2 \to \infty$, Φ approaches a non-zero finite value. In this case, Π_2 becomes immaterial, and the function Φ can be replaced with its limiting value. This is called *complete similarity*, or *similarity of the first kind in the parameter* Π_2. This behaviour is the type of Reynolds number similarity often assumed in analysis of turbulent flow, including von Kármán's arguments which lead to the logarithmic 'law of the wall'.

(*b*) As $\Pi_2 \to \infty$, Φ asymptotically approaches a power-law dependence on the parameter Π_2, taking on the property of generalized homogeneity:

$$\Phi = \Pi_2^{\alpha_1} \Phi_1(\Pi_1 \Pi_2^{\alpha_2}). \tag{7.1}$$

This is called *incomplete similarity*, or *similarity of the second kind in the parameter* Π_2. This is the type of similarity recently proposed by Barenblatt (1993) and Barenblatt & Prostokishin (1993) as an alternative to the logarithmic 'law of the wall'.

(*c*) Neither *a* or *b* holds, and there is no self-similarity.

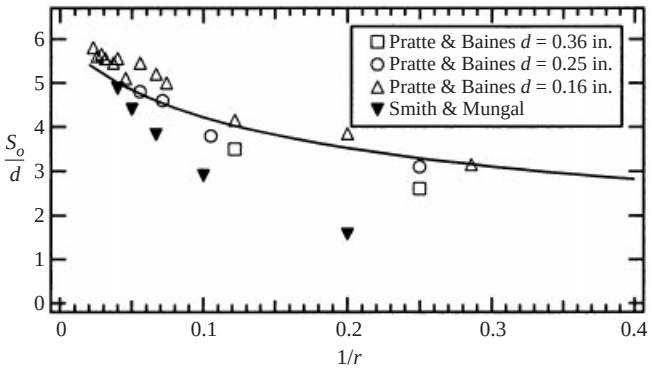

FIGURE 12. Prediction of potential core length compared with data from Pratte & Baines (1967) and Smith & Mungal (1998).

Case *b* is a more difficult situation than case *a*, because of the additional task of determining α_1 and α_2. In the present work, we have assumed complete similarity in the wake-scaling region of the jet, and shown good agreement to data when $r \gg 1$. However, we have also shown that agreement is less perfect when r is smaller. Thus we have not ruled out that the similarity is not of the second kind. To prove this, however, would require the introduction of the exponents α_1 and α_2, which would probably have to be experimentally determined. Although this approach might provide a more unified theory (applicable to a much wider range of r), pursuing this possibility is beyond the scope of the present work.

The authors would like to acknowledge J. E. Broadwell for many inspirational discussions, and S. H. Smith for providing the scalar imaging data. This work was supported by the Gas Research Institute, R. V. Serauskas, Technical Monitor.

Appendix. A simple prediction of the length of the potential core

A simple method to estimate the length of the potential core of transverse jets can be derived based on the entraining vortex sheet model of Coelho & Hunt (1989). This length is a lower bound to the distance from the jet nozzle over which any type of similarity might be expected.

Coelho & Hunt (1989) derived an expression for the perturbation of an initially annular vortex sheet issuing from a jet nozzle into a crosswind. The vortex sheet is superposed with a sink sheet, whose strength is proportional to the local slip velocity across the sheet, in order to mimic near-field entrainment. The perturbation of the sheet from an initially perfect circle, normalized by jet diameter, is given in terms of azimuthal angle θ (measured from the leading edge of the nozzle), the entrainment coefficient ϵ, axial distance from the nozzle, s, and the crossflow-to-jet velocity ratio, $\lambda = v_\infty/u_j = \frac{1}{r}(\rho_j/\rho_\infty)^{1/2}$:

$$R' = s\epsilon + (1 + k')s^2 \cos\theta\epsilon\lambda + O(\lambda^2, \epsilon^2, \lambda^2, \epsilon\lambda^2 \ldots). \tag{A 1}$$

Here k' is a constant which is presumed to be small; all distances are normalized by jet diameter in this expression. Supposing that the potential core is ended when the maximum ($\theta = 0$ or π) perturbation reaches a critical value: we have

$$s_o\epsilon + s_o^2\epsilon\lambda = \zeta_{crit}, \tag{A 2}$$

where ζ_{crit} is a constant, and s_o denotes the end of the potential core. For free jets, the potential core is approximately six diameters in length. Hence $\zeta_{crit}/\epsilon = 6$, and so

$$s_o = \frac{-1 \pm (1 + 24\lambda)^{1/2}}{2\lambda}. \tag{A 3}$$

A comparison of this expression with the velocity results of Pratte & Baines (1967) is shown in figure 12. Agreement is good for a large range of velocity ratios and jet diameters. The scalar concentration data of Smith & Mungal (1998), however, shows potential cores which are somewhat shorter.

REFERENCES

Abramovich, G. N. 1963 *Theory of Turbulent Jets*. MIT Press.

Andreopoulos, J. & Rodi, W. 1985 On the structure of jets in crossflow. *J. Fluid Mech.* **138**, 93–127.

Barenblatt, G. I. 1993 Scaling laws for fully developed turbulent shear flows. Part 1. Basic hypothesis and analysis. *J. Fluid Mech.* **248**, 513–520.

Barenblatt, G. I. 1996 *Scaling, Self-similarity, and Intermediate Asymptotics*. Cambridge University Press.

Barenblatt, G. I. & Prostokishin, V. M. 1993 Scaling laws for fully developed turbulent shear flows. 2. processing of experimental data. *J. Fluid Mech.* **248**, 521–529.

Barenblatt, G. I. & Zel'dovich, Y. B. 1972 Self-similar solutions as intermediate asymptotics. *Ann. Rev. Fluid Mech.* **4**, 285–312.

Batchelor, G. K. 1967 *An Introduction to Fluid Dynamics*. Cambridge University Press.

Broadwell, J. E. & Breidenthal, R. E. 1984 Structure and mixing of a transverse jet in incompressible flow. *J. Fluid Mech.* **148**, 405–412.

Cantwell, B. J. 1981 Organized motion in turbulent flow. *Ann. Rev. Fluid Mech.* **13**, 457–515.

Chang, Y. K. & Vakili, A. D. 1995 Dynamics of vortex rings in crossflow. *Phys. Fluids* **7**, 1583–1597.

Chassaing, P., George, J., Claria, A. & Sananes, F. 1974 Physical characteristics of subsonic jets in a cross-stream. *J. Fluid Mech.* **62**, 41–64.

Chen, C. J. & Rodi, W. 1980 *Vertical Turbulent Buoyant Jets: A Review of Experimental Data*. Pergamon.

Coelho, S. L. V. & Hunt, J. C. R. 1989 The dynamics of the near field of strong jets in crossflows. *J. Fluid Mech.* **200**, 95–120.

Durando, N. A. 1971 Vortices induced in a jet by a subsonic cross flow. *AIAA J.* **9**, 325–327.

Eroglu, A. & Breidenthal, R. E. 1991 Effects of periodic disturbances on structure and flame length of a jet in a cross flow. *AIAA Paper* 91-0317.

Fearn, R. L. & Weston, R. P. 1974 Vorticity associated with a jet in a cross flow. *AIAA J.* **12**, 1666–1671.

Fearn, R. L. & Weston, R. P. 1975 Induced pressure distribution of a jet in a crossflow. *Tech. Rep.* TN D-7916. NASA.

Fric, T. F. & Roshko, A. 1994 Vortical structure in the wake of a transverse jet. *J. Fluid Mech.* **279**, 1–47.

Gogineni, S., Goss, L. & Roquemore, M. 1995 Manipulation of a jet in a crossflow. *Exp. Therm. Fluid Sci.* **16**, 209–219.

Gollahalli, S. R., Brzustowski, T. A. & Sullivan, H. F. 1975 Characteristics of a turbulent propane diffusion flame in a cross-wind. *Trans. Can. Soc. Mech. Engng* **3**, 205–214.

Hasselbrink, E. F. & Mungal, M. G. 1996 An analysis of the time-averaged properties of the far field of the transverse jet. *AIAA Paper* 96-0201.

Hasselbrink, E. F. & Mungal, M. G. 2001 Transverse jets and jet flames. Part 2. Velocity and OH field imaging. *J. Fluid Mech.* **443**, 27–68.

Hoult, D. P. & Weil, J. C. 1972 Turbulent plume in a laminar cross flow. *Atmos. Environ.* **6**, 513–531.

Kamotani, Y. & Greber, I. 1972 Experiments on a turbulent jet in a cross flow. *AIAA J.* **10**, 1425–1429.

KARAGOZIAN, A. R. 1986 An analytical model for the vorticity associated with a transverse jet. *AIAA J.* **24**, 429–436.

KARAGOZIAN, A. R. & NGUYEN, T. T. 1986 Effects of heat release and flame distortion in the transverse fuel jet. In *Twenty-First Symp. (Intl) on Combustion*, pp. 1271–1279. The Combustion Institute.

KEFFER, J. F. & BAINES, W. D. 1963 The round turbulent jet in a cross wind. *J. Fluid Mech.* **15**, 481–496.

KELSO, R. M., LIM, T. T. & PERRY, A. E. 1996 An experimental study of round jets in cross-flow. *J. Fluid Mech.* **306**, 111–144.

KUZO, D. M. 1995 An experimental study of the turbulent transverse jet. PhD thesis, California Institute of Technology.

MARGASON, R. J. 1968 The path of a jet directed at large angles to a subsonic free stream. *Tech. Rep.* TN D-4919. NASA.

MARGASON, R. J. 1993 Fifty years of jet in crossflow research. In *AGARD Symp. on a Jet in Cross Flow, Winchester, UK, AGARD CP*–534.

MOUSSA, Z. M., TRISCHKA, J. W. & ESKINAZI, S. 1977 The near field in the mixing of a round jet with a cross-stream. *J. Fluid Mech.* **80**, 49–80.

PATRICK, M. A. 1967 Experimental investigation of the mixing and penetration of a round turbulent jet injected perpendicularly into a transverse stream. *Trans. Inst. Chem. Engrs* **45**, 16–31.

PRATTE, B. D. & BAINES, W. D. 1967 Profiles of the round turbulent jet in a cross flow. *J. Hydraul. Div., ASCE* **92** (HY6), 53–64.

RICOU, F. P. & SPALDING, D. B. 1961 Measurements of entrainment by axisymmetrical turbulent jets. *J. Fluid Mech.* **11**, 21–32.

SCORER, R. S. 1958 *Natural Aerodynamics*. Pergamon.

SMITH, S. H. 1996 The scalar concentration field of the axisymmetric jet in crossflow. PhD thesis, Stanford University.

SMITH, S. H. & MUNGAL, M. G. 1998 Mixing, structure and scaling of the jet in crossflow. *J. Fluid Mech.* **357**, 83–122.

SYKES, W., LEWELLEN, W. & PARKER, S. 1986 On the vorticity dynamics of a turbulent jet in a crossflow. *J. Fluid Mech.* **168**, 393–413.

YUAN, L. L., STREET, R. L. & FERZIGER, J. H. 1999 Large eddy simulations of a round jet in crossflow. *J. Fluid Mech.* **379**, 71–104.